Materials Chemistry and Physics 334 (2025) 130463

Contents lists available at ScienceDirect

Materials Chemistry and Physics

journal homepage: www.elsevier.com/locate/matchemphys

Revealing the nature of the Zn_2GeO_4 bluish-white emission in microwave-assisted hydrothermal synthesized nanorods

Miguel P. Dias [a], Maria S. Batista [a], Ana Pimentel [b], Elvira Fortunato [b], Rodrigo Martins [b], Florinda M. Costa [a], Sónia O. Pereira [a], Joana Rodrigues [a,*], Teresa Monteiro [a]

[a] i3N/UA, Department of Physics, University of Aveiro, 3810-193, Aveiro, Portugal
[b] i3N/CENIMAT, Department of Materials Science, NOVA School of Science and Technology, Campus de Caparica, 2829-516, Caparica, Portugal

HIGHLIGHTS

- Zn_2GeO_4 nanorods synthesized via a microwave-assisted hydrothermal method.
- Estimated energy bandgap of 5.25 eV at room temperature.
- Bluish-white structureless broad emission band observed at ca. 480 nm (~2.58 eV).
- Overlap of two emitting centers: intrinsic defect (BL) and Mn^{2+} intraionic transition (GL).
- Persistent luminescence from the Mn^{2+} GL recorded for at least 5 s.

ARTICLE INFO

Keywords:
Zinc germanate
Nanorods
Doping
Persistent luminescence
Defects

ABSTRACT

Recently, zinc germanate (Zn_2GeO_4, ZGO) has emerged as a material with significant potential for various applications due to its unique optical properties. Undoped, manganese (Mn) and and chromium (Cr)-doped ZGO were synthesized through microwave-assisted hydrothermal methods. The as-synthesized and thermal annealed materials were morphological and structurally characterized, and the optical properties of these willemite prismatic nanorods were thoroughly investigated. A room temperature (RT) bandgap energy close to 236 nm (~5.25 eV) was obtained, which is slightly higher than the values reported so far in the literature. Furthermore, optically active absorption and luminescence bands from the ultraviolet to near-infrared were identified. All samples present intrinsic defect absorption with a maximum at 271 nm (~4.58 eV) and a charge transfer Mn^{2+}-O^{2-} absorption band at 315 nm (~3.94 eV). In addition, the so-called bluish-white structureless broad emission band is observed at RT at ca. 480 nm (~2.58 eV) for all the analyzed samples. Our investigation indicates that this band is due to the overlap of two emitting centers: an intrinsic defect originating a blue luminescence (BL) and the $^4T_1 \rightarrow {}^6A_1$ intraionic transition of Mn^{2+} leading to a green luminescence (GL), confirming Mn as a common contaminant in this matrix. For the Cr-doped samples, the thermal annealing treatment was seen to promote changes in the visible and near infrared (NIR) intraionic absorption bands. This enabled the identification of the presence of trivalent and tetravalent Cr ion charge states. Additionally, temperature-dependent photoluminescence measurements were carried out in the case of the as-synthesized ZGO:Mn, which is the sample with the highest GL intensity. It was found that the intensity of GL decreases with temperature (from 18 K to RT), with a thermal activation energy of 18 ± 2 meV for the nonradiative processes that compete with the observed luminescence. Moreover, persistent emission from the Mn^{2+} GL was recorded for at least 5 s and was attributed to multi-trapping/de-trapping processes occurring at different trap depths, which are responsible for the distinct decays observed.

---

* Corresponding author.
E-mail address: joana.catarina@ua.pt (J. Rodrigues).

https://doi.org/10.1016/j.matchemphys.2025.130463
Received 15 October 2024; Received in revised form 6 January 2025; Accepted 25 January 2025

1. Introduction

Zinc germanate (Zn_2GeO_4), hereafter designated as ZGO, appears as a material of particular interest due to its unique properties and potential for innovation in various fields, including information storage, anti-counterfeiting, photocatalysis, and bioimaging, to name a few applications [1–4]. With a reported direct wide bandgap energy in the range of 4.4–4.9 eV [2,5–7], this oxide semiconductor is known to exhibit high thermal stability and shows promise for the development of ultraviolet (UV) photodetectors. Additionally, it exhibits bright room temperature (RT) luminescence in the visible spectral region and has significant potential for persistent luminescence (PersL), which opens up further applications such as fluorescence latent fingerprinting imaging, among others [8–11]. Despite its advantages, the identification of optically active defects in ZGO is still in an early stage and has been the topic of debate within the scientific community [3,5,6,8,9]. ZGO, with its willemite crystalline structure, contains numerous intrinsic defect levels that span through the material's bandgap [5,6]. These defects, along with trace impurities, complicate the full understanding of its optical properties. The material can be grown or synthesized using different high- and low-temperature approaches, leading to the development of distinct defects. This variety makes it challenging to trace the luminescence, as several optical active centers may coexist in the same spectral region. Doping the materials enhances and controls their optical properties; hence, selecting a suitable doping ion is essential for the emission range required for the desired applications. For instance, Cr and Mn ions are popular choices for bioimaging and anti-counterfeiting applications, respectively [12].

This study investigates the morphological, structural, and optical properties of ZGO nanorods synthesized using the microwave-assisted hydrothermal method. Nominally undoped, and doped with Mn (ZGO:Mn) and Cr (ZGO:Cr) ZGO nanorods were synthesized at 170 °C and further submitted to thermal annealing treatments in air at 400 °C. All the samples, except for the as-synthesized ZGO:Mn, exhibit a pure willemite crystalline phase as confirmed by X-ray diffraction (XRD) and Raman spectroscopy. RT absorption indicates a higher bandgap energy than the ones previously reported in several works [2,5–7]. Additionally, the absorption spectra reveal bands related to trace and intentionally introduced Mn and Cr impurities. Photoluminescence (PL) and photoluminescence excitation (PLE) studies evidence that when excited near the band edge, both the as-synthesized and annealed samples exhibit a bright bluish-white structureless emission band. This band has a maximum at 480 nm at RT and extends from the UV to the red spectral region, consistent with previous observations [3,5,13,14]. The present work demonstrates that this broad emission band results from the overlap of two distinct emitting centers, one of them originating a blue luminescence (BL), likely related to an intrinsic defect, while the other generates green luminescence (GL), assigned to the intraionic ${}^4T_1 \rightarrow {}^6A_1$ Mn^{2+} transition. Mn^{2+} is known to substitute Zn^{2+} sites in the ZGO lattice due to the radii similarity (0.60 Å and 0.66 Å for Zn^{2+} and Mn^{2+}, respectively, in tetrahedral coordination) [3,15–17]. The bright Mn^{2+} GL is observed with the naked eye at RT. The temperature dependence of the GL was further evaluated from 18 K to RT and the nonradiative processes that compete with the radiative ones are well described by a classical model considering an activation energy of 18 meV.

The ZGO and ZGO:Mn nanorods prepared in this study exhibited a bluish-white and green PersL after ceasing the UV excitation at 271 nm, showing an afterglow that lasted for more than 50 ms (observed with the naked eye). This energy-saving low-temperature synthesis shows promise for producing tailored doped nanostructures with high potential for luminescence-based anti-counterfeiting and bioimaging applications, among others.

2. Experimental details

Zn_2GeO_4 nanorods were synthesized using a microwave-assisted hydrothermal method based on the one performed by Yang et al. [18]. All synthesis reactions were made using only water as the solvent (a green solvent). Hydrothermal synthesis is extensively used to promote the preferred growth of some nanostructures such as nanorods, nanoflowers and microspheres. The use of microwave irradiation facilitates the production of a more uniform nanoparticle in size and morphology, by offering a more homogeneous reaction environment.

Firstly, 1.190 g of zinc nitrate hexahydrate ($(Zn(NO_3))_2 \cdot 6H_2O$, 98 %, CAS:10,196-18-6, from Acros Organics) and 3.604 g of urea ($(NH_2)_2CO$, 98 %, CAS:57-13-6, from FisherChemical) were dissolved in 35 mL of deionized H_2O under stirring until the solution was transparent. Then, 0.209 g of germanium oxide (GeO_2, 99.99 %, CAS: 1310-53-8, from Sigma-Aldrich) was added to the solution, which was then stirred for another 20 min. Afterward, the resulting white colloidal solution was transferred to a microwave Teflon vessel, sealed, and maintained at 170 °C for 10 min using a multi-mode Microwave synthesizer (Mars one, from CEM).

For the Mn and Cr doped samples, manganese (II) acetate tetrahydrate ($Mn(CH_3COO)_2 \cdot 4H_2O$, 99 %, CAS: 6156-78-1, from Sigma-Aldrich) and chromium (III) chloride hexahydrate ($CrCl_3 \cdot 6H_2O$, 96 %, CAS:10,060-12-5, from Sigma-Aldrich), respectively, were used in a concentration of 10 mol%.

After the reaction, the vessels were cooled down to RT. The as-prepared precipitates were washed with deionized H_2O followed by isopropanol and centrifuged at 4000 rpm for 5 min several times. The powders were dried in air at RT for 72 h before their characterization. To further investigate the effect of heat treatment on these samples, all the prepared powders were annealed in air at 400 °C for 1 h.

The morphology of the as-synthesized and annealed ZGO nanorods was assessed through scanning electron microscopy (SEM) using a Hitachi Regulus 8220 Scanning Electron Microscope (Mito, Japan).

XRD and RT Raman spectroscopy were used to evaluate the structural properties of the as-synthesized and annealed nanorods. XRD experiments were conducted using a PANalytical's X'Pert PRO MPD diffractometer (Almelo, The Netherlands) equipped with an X'Celerator detector and using CuK_α radiation ($\lambda = 1.540598$ Å). The data were recorded from 15° to 70° 2θ range with a step of 0.033° in the Bragg–-Brentano configuration. Raman spectroscopy measurements were performed at RT using a Horiba Jobin Yvon HR800 spectrometer, under backscattering configuration, with an objective of × 50 magnification and with a 600 grooves mm^{-1} grating, using a 532 nm laser line as the excitation source (Ventus-LP-50085, Material Laser Quantum).

Diffuse reflectance measurements were performed at RT using a UVVIS JASCO V-780 spectrometer with an integrated sphere JASCO ISN-901i in the wavelength range 190–1600 nm, with a bandwidth of 5 nm and a speed velocity of 100 nm min^{-1}. Absorption spectra were obtained by applying the Kubelka-Munk function [19,20] to the measured diffuse reflectance data.

The optical properties of the produced samples were assessed by PL and PLE at RT by a Fluorolog®-3 from Horiba Scientific. A 450 W Xenon lamp (continuous) was used as the excitation source, coupled with a double additive grating monochromator, Gemini 180, with a diffraction grating of 1200 grooves mm^{-1} and 2 × 180 mm, in the excitation side and a triple grating iHR550 spectrometer in the emission, with 1200 grooves mm^{-1} and 550 mm. An R928P PMT detector sensitive to wavelengths from 200 to 850 nm, was used.

Additionally, temperature-dependent PL measurements were carried out using a SPEX 1074 Czerny-Turner as a monochromator, with a diffraction grating of 1200 grooves mm^{-1} and a focal distance of 1 m. For these measurements, the samples were placed on a cold finger He cryostat, under vacuum conditions, which allows for varying the temperature from ~18 K up to RT. The samples were excited using the 325 nm (~3.81 eV) line of a He–Cd laser and the luminescence was detected with a water-cooled Hamamatsu R928 photomultiplier. The optical alignment at a 90-degree geometry between sample irradiation and signal detection was ensured during the conduction of these studies.

To study the evolution of the intensity of the PersL with the time (afterglow), the same Fluorolog®-3 was used in the kinetics mode. The samples were irradiated with the 450 W Xe lamp, mentioned above, for 10 min with a wavelength of 271 nm, after which the irradiation source was turned off and the decay curves were acquired for different periods.

3. Results and discussion

The SEM images of the as-synthesized and annealed ZGO, ZGO:Mn, and ZGO:Cr are shown in Fig. 1. The morphology of the nominally undoped ZGO (Fig. 1-a)) consists of prismatic rods with an average length of approximately 538 ± 142 nm and a width of around 104 ± 29 nm. Additionally, some agglomerates ranging from 100 to 1000 nm and partially formed rods measuring between 100 and 400 nm in length were also observed. After annealing (Fig. 1-b)), a reduction in the number of agglomerates is seen and the rods appear much smoother with more uniform sizes. Larger rods, with lengths around 900 nm, were also noted. On average, the dimensions of the nanorods increased to 654 ± 239 nm in length and 116 ± 40 nm in width, respectively. Fig. 1-c) evidenced that most of the ZGO:Mn rods are still being formed under the employed synthesis conditions. It indicates a higher number of rod agglomerates with an average length of 437 ± 158 nm and an average width that is thinner than the undoped ZGO (73 ± 27 nm). After annealing (Fig. 1-d)), the ZGO:Mn rods exhibited some clustering and increased in both length and thickness, presenting an average length of 473 ± 251 nm and width of 141 ± 77 nm. For the ZGO:Cr sample (Fig. 1-e)), rod formation is evident; however, a significant number of particle agglomerates of around 1 μm of diameter are detected. In this case, the nanorods are shorter than the undoped ZGO (270 ± 81 nm), with an average width similar to the Mn-doped sample (68 ± 16 nm). After the heat treatment (Fig. 1-f)), many agglomerates and clusters were observed, increasing the average length and width of the nanorods

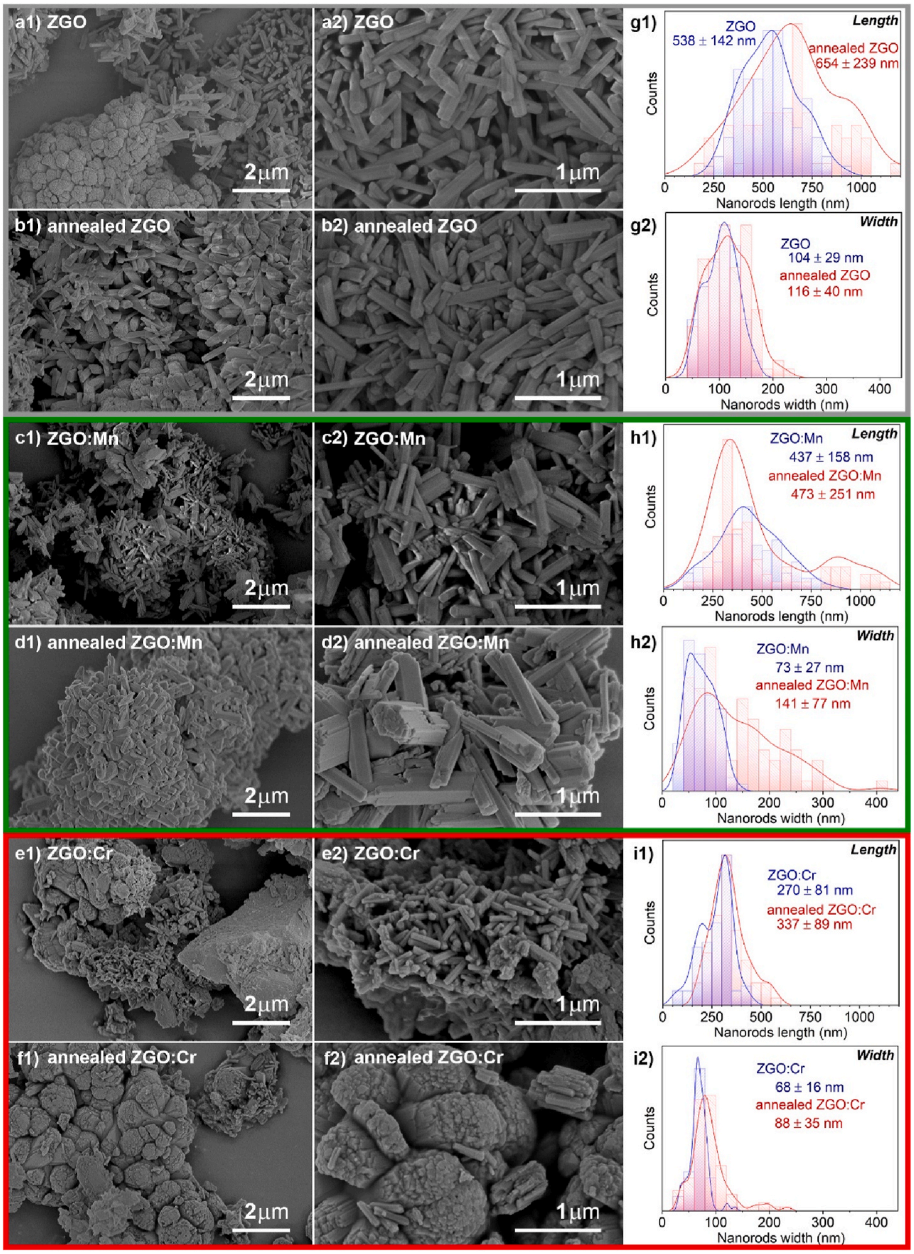

Fig. 1. SEM images and particle size distribution maps: a), b) SEM images with different magnification factors of ZGO before and after annealing; c), d) the corresponding SEM images for ZGO:Mn before and after annealing; and e), f) SEM images for ZGO:Cr before and after annealing; 1 and 2 denote the different magnifications used; g), h), i) size distribution histograms of the length (1) and width (2) of the nanorods before and after the annealing treatment.

to 337 ± 89 nm and 88 ± 35 nm, respectively.

As evidenced, the synthesis conditions lead to the creation of nano/microrods and agglomerates. Overall, the thermal annealing treatment induces the formation of smoother, longer, and thicker rods and dispersed agglomerates. In addition, rods are more easily formed in nominally undoped ZGO, followed by ZGO:Mn and ZGO:Cr. The latter shows more agglomerates after the same synthesis and annealing conditions.

The structural properties of the samples were assessed by XRD and Raman spectroscopy as shown in Fig. 2. The X-ray diffractograms displayed in Fig. 2-a) indicate that for the as-synthesized ZGO and ZGO:Cr, and annealed ZGO, ZGO:Mn and ZGO:Cr rods exhibit a monophasic structure with a pure willemite crystalline phase, consistent with the patterns of the JCPDS No. 11–0687 card. In contrast, the as-synthesized ZGO:Mn shows extra diffraction maxima, particularly at around 31.8°, which could correspond to either JCPDS No. 24–0734, i.e. to tetragonal manganese oxide (Mn_3O_4), or to JCPDS No. 36–1451, i.e. to wurtzite zinc oxide (ZnO). Nevertheless, the thermal annealing process effectively removes the extra residual crystalline phase, resulting in a monophasic sample, similar to the others. In addition, thermal annealing caused a slight shift of the diffraction maxima to smaller angles (Fig. 2-a) *inset*), particularly for the ZGO:Mn and ZGO:Cr samples. This shift indicates a modest increase in the interplanar distance, in line with previous reports regarding the radii difference between the dopants and Zn lattice ions, which confirms the effective doping of the samples [3]. Moreover, the shift was more pronounced for the Mn-doped sample, as anticipated, given that the difference between the radii of Mn^{2+} (0.66 Å) and Zn^{2+} (0.60 Å) is also greater than the difference between both Cr^{3+} (0.61 Å) and Zn^{2+} and Cr^{4+} (0.41 Å) and Ge^{4+} (0.39 Å) [3,15–17,21,22].

The crystalline structure of the samples was further confirmed by RT Raman spectra shown in Fig. 2-b). All samples exhibit dominant vibrations in the high-frequency region, with maxima at ca. 801 cm^{-1} ($A_g^{(2)}$), 775 cm^{-1} ($E_g^{(4)}$), 751 cm^{-1} ($E_g^{(3)}$) and 745 cm^{-1} ($A_g^{(1)}$). These vibrational modes account well for the stretching vibration of O-Ge-O in GeO_4 tetrahedra, Ge-O-Zn asymmetric, defect oxygen mode, and Ge-O-Zn symmetric vibrations, respectively, in line with what has been reported [6,18,23].

The RT absorption, PL, and PLE spectra of the investigated nanorods are displayed in Fig. 3. As shown in Fig. 3-a), in the studied spectral range, the as-synthesized and thermal annealed ZGO mainly present ultraviolet absorption for wavelengths shorter than 350 nm (~3.54 eV). These samples evidence an absorption shoulder ca. 294 nm (~4.22 eV), followed by a steeper absorption peaked at 236 nm (~5.25 eV). In addition, an absorption band at higher energies is also observed, with a maximum at 214 nm (~5.79 eV). These three absorption bands are observed in all the samples under investigation.

As mentioned, the bandgap energy for this direct oxide host has been reported between 4.4 and 4.9 eV [2,5–7]. However, our findings indicate that the studied nanorods exhibit a higher bandgap energy. In the near band edge spectral region, several overlapping absorption bands hamper a precise assignment of the bandgap energy. Therefore, we will assume that it corresponds to the most intense absorption peaked at around 5.25 eV. Nevertheless, as a higher energy absorption band was observed, its association with the bandgap of the material cannot be fully discarded. As it will be further discussed, the shoulder at 294 nm (~4.22 eV) was attributed to an overlap of an intrinsic defect absorption band with a maximum at 271 nm (~4.58 eV) with the absorption to the Mn^{2+}-O^{2-} charge transfer state (CTS) at 315 nm (~3.94 eV) [3,16]. This means that the CTS energy level is around 1.3 eV below the minimum of the conduction band. The presence of the CTS in all the studied samples indicates that even the nominally undoped ZGO presents Mn impurities as a trace contaminant, likely to arise from the used synthesis precursors. Fig. 3-a) also shows two absorption bands with maxima at 434 nm (~2.86 eV) and 597 nm (~2.08 eV), both found for the ZGO:Cr samples. These bands match well with the predicted lowest energy ${}^4A_2 \rightarrow {}^4T_1$ and ${}^4A_2 \rightarrow {}^4T_2$ Cr^{3+} transitions for the ion in octahedral coordination when placed in sites with intermediate crystal field strength [24,25]. For longer wavelengths, a pronounced absorption between 600 and 1200 nm is assigned to ${}^3A_2 \rightarrow {}^3T_1$ and ${}^3A_2 \rightarrow {}^3T_2$ transitions of Cr^{4+} when the ion is placed in a lower symmetry site than the cubic one, as happens for instance for other germanate hosts, such as Mg_2GeO_4 [26]. From the comparison between the absorption spectra of the ZGO:Cr and ZGO:Mn samples, it can be inferred that the as-synthesized Mn-doped sample contains Cr impurities in its composition. Additionally, the thermal annealing at 400 °C helps to optically activate the Cr^{4+} ions, in contrast to the Cr^{3+} ion transitions observed in the ZGO:Cr sample before the heat treatment. Moreover, both the Mn and Cr doped and annealed ZGO monophasic nanorods evidenced an absorption band centered around 372 nm (~3.33 eV). This band is likely related to Cr^{4+} absorption since it only appears in the annealed samples.

The RT PL and PLE showed in Fig. 3-b) reveal that the dominant recombination of the as-synthesized ZGO corresponds to a broad structureless emission band centered ca. 480 nm (~2.58 eV) and spanning from the UV to the red spectral region, resulting in a bluish-white bright luminescence under UV excitation. As seen from the PLE spectrum monitored at the emission band maximum, and within the assessed spectral range, the bluish-white luminescence is preferentially populated via a broad excitation band peaked at 271 nm (~4.58 eV). This band was assigned to the intrinsic defect excitation band, eventually associated with the oxygen vacancies (V_O)-related absorption. This

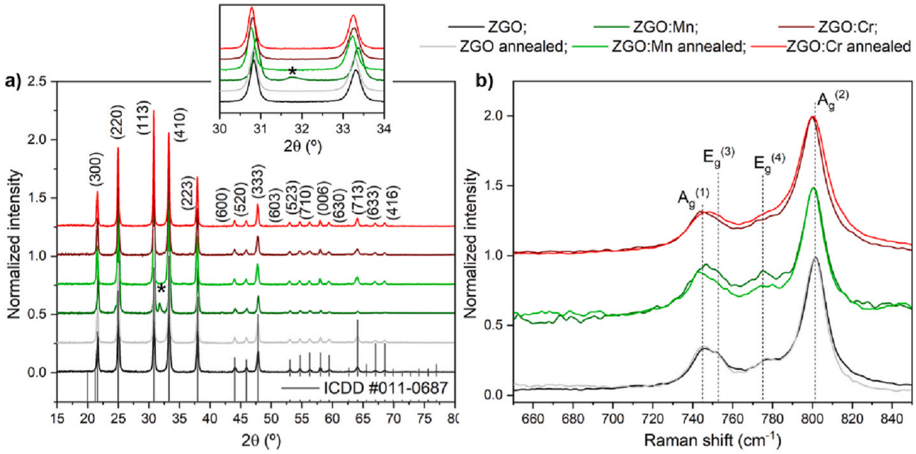

Fig. 2. a) Normalized XRD patterns (*inset* shows with detail the shift of the diffraction maxima), and b) Normalized RT Raman spectra, obtained with the 532 nm laser line, for the as-synthesized and annealed ZGO, ZGO:Mn and ZGO:Cr nanorods. In a) and b) the spectra were vertically shifted for clarity. The spectra were normalized to the respective intensity maxima.

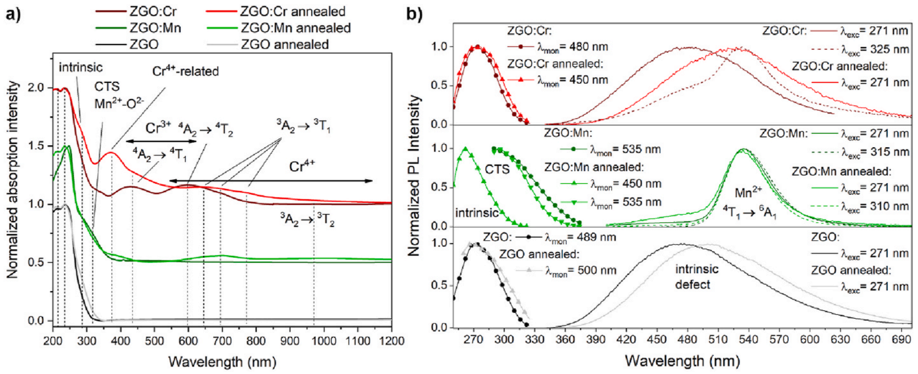

Fig. 3. a) RT normalized absorption spectra and b) normalized PL (full and dashed lines) and PLE (full lines with symbols) spectra of as-synthesized and annealed ZGO, ZGO:Mn, and ZGO:Cr samples. The spectra were normalized to the intensity maxima and, in a) the spectra were vertically shifted for clarity.

interpretation aligns with predictions made using density functional theory (DFT) [5,27]. The blue emission band has been attributed to the recombination of intrinsic defects such as V_O or interstitial zinc (Zn_i) along with an acceptor defect [3,5,14], as noted in the literature. After thermal annealing, the emission band of ZGO is red-shifted, peaking at 500 nm (~2.48 eV). Additionally, the PLE spectrum exhibits an excitation band peaked at 271 nm (~4.58 eV); however, this band is broader than that observed in the non-annealed sample, suggesting that the excitation band may result from the overlap of excitation bands. For the ZGO:Mn samples, the spectra displayed in Fig. 3-b) allowed us to conclude that the emission consists of a narrower band centered in the green spectral region, at 535 nm (~2.32 eV). This corresponds to the characteristic intraionic $^4T_1 \rightarrow {}^6A_1$ emission of Mn^{2+} [3,10,11,13,15–17,22]. Yet, when excited within the PLE maxima (271 nm), the bluish-white band can still be identified, although with much less intensity than the green luminescence (GL) of Mn^{2+}. In addition, the PLE spectrum monitored at 535 nm (~2.32 eV) shows that the Mn^{2+} GL is preferentially populated with photons of 315 nm (~3.94 eV), that is, via photon absorption on the Mn^{2+}-O^{2-} CTS. Nevertheless, the GL is also populated via the intrinsic defect-related excitation band. Therefore, the PLE spectra of the monitored blue and green bands indicate the presence of the overlap of an excitation/absorption band due to the intrinsic-related defect and the Mn^{2+}-O^{2-} CTS excitation/absorption band. This means that by using 271 nm or 315 nm excitation both emitting defects can be excited, leading to the bluish-white color perception.

In the case of the Cr-doped samples, upon excitation within Cr-related absorption bands, no visible Cr^{3+} nor near-infrared Cr^{4+} intra-ionic transitions were detected at RT. As before, the main recombination/excitation process shown in the PL and PLE spectra, displayed in Fig. 3-b), evidence that the dominant emission bands are the blue/bluish-white and green emission bands due to the intrinsic defect and Mn^{2+} impurity, respectively. In addition, the spectral overlap of the emitting centers is evident, particularly from the PL spectrum acquired with the 325 nm (~3.81 eV) excitation. Therefore, our measurements support the identification of two main overlapping optically active defects: one of intrinsic nature and the other extrinsic, with emission peaks at 480 nm (~2.58 eV) and 535 nm (~2.32 eV), respectively. The distinct

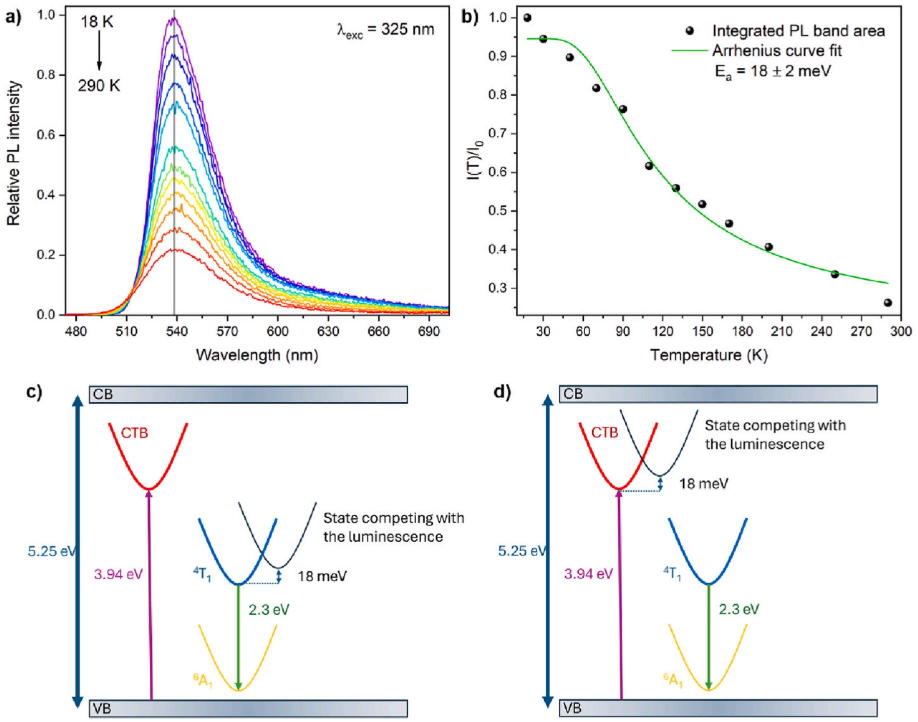

Fig. 4. a) Temperature dependence of the $^4T_1 \rightarrow {}^6A_1$ Mn^{2+} GL for ZGO:Mn sample. The spectra were obtained with 325 nm photon excitation (~3.81 eV). b) Evolution of the PL integrated intensity with temperature; c) and d) schematic representation of models to describe the luminescence thermal quenching effects.

intensity ratio between these two emitting centers accounts for the shifts in the PL maxima that were observed.

To obtain a deeper insight into the quenching mechanisms of the intraionic $^4T_1 \rightarrow ^6A_1$ Mn^{2+} emission, the sample with the highest GL intensity (the as-synthesized ZGO:Mn) was chosen to evaluate the temperature-dependent PL. The corresponding spectra from 18 K to RT obtained with 325 nm (~3.81 eV) excitation, i.e., by exciting the sample into the Mn^{2+}-O^{2-} CTS absorption, are shown in Fig. 4. As seen in Fig. 4-a), with increasing temperatures, a thermal quenching of the $^4T_1 \rightarrow ^6A_1$ Mn^{2+} GL intensity is observed. At RT, the emission intensity corresponds to nearly 26 % of its initial value at 18 K. The band shape was seen to enlarge when raising the temperature and no shift in the peak position was observed. The temperature dependence of the GL integrated intensity shown in Fig. 4-b) reveals that the non-radiative processes that compete with the radiative ones are well accounted for a classical model [28],

$$I(T) \Big/ I_0 = [1 + C\,exp\,(-E_a/k_BT)]^{-1}$$

in which $I(T)$ is the integrated PL intensity at a given temperature T, I_0 is the integrated area of the PL intensity at low temperature, E_a stands for the thermal activation energy for the non-radiative processes, k_B to the Boltzmann constant and C is a weighting factor, considered as a constant and expressing the ratio between the radiative lifetime and a value related to the nonradiative lifetime of carriers. The best fit to the data shown in Fig. 4-b) was achieved using an activation energy of 18 ± 2 meV. From this data, two main hypotheses can be considered to explain the observed phenomenon: i) the existence of a nonradiative electronic level located at 18 ± 2 meV above the $^4T_1$ emitting level (Fig. 4-c)), or ii) a nonradiative level located ca. 18 meV above the CTS state (Fig. 4-d)). This would mean that by raising the temperature some electrons on the Mn^{2+} emitting state will instead be excited to one of those states. Nevertheless, we cannot rule out other hypotheses at this stage, such as the possibility of energy transfer between distinct defects in the ZGO:Mn lattice. Notably, the comparison between the PL and absorption spectra reveals that the emission from Mn^{2+} partially overlaps with the absorption of chromium ions. This overlapping suggests that energy transfer between the two ions can take place.

Fig. 5-a) shows the decay of the luminescence intensity in ZGO:Mn after 10 min of excitation with 271 nm (~4.58 eV) photons, monitored at the maximum of the Mn^{2+} GL. During excitation, defect centers can trap charge carriers, storing the energy from the optical excitation. When the excitation light is turned off, this stored energy is then released to the emitting centers. Indeed, upon excitation at the intrinsic/Mn^{2+}-O^{2-} CTS excitation/absorption bands, charge carriers are captured, and the subsequent release of the trapped electrons to the defect emitting levels leads to the observation of the green luminescence from Mn^{2+}.

As seen, the measured time dependence of the luminescence intensity after ceasing the excitation light (afterglow) is higher than expected for the radiative decay time of the spin-forbidden $^4T_1 \rightarrow ^6A_1$ Mn^{2+} transition, which is likely to be in the order of a few milliseconds. In addition, the afterglow decay curve cannot be described by a single (or multiple) exponential function(s). The best fit to the experimental data shown in Fig. 5-a) was obtained by using a sum of four stretched exponential functions, along with a dispersion factor δ ($0 < \delta < 1$) to describe disordered systems due to the diffusion of photoexcited carriers [27]. The faster decay from the $^4T_1$ emitting state, which is 22 ms, is likely to be associated with the radiative lifetime. In contrast, the longer decays of 152 ms, 675 ms, and 2533 ms are probably related to the duration that the carriers spend in the traps. It is also noteworthy that the first three estimated lifetimes correspond to simple exponential functions, whereas the dispersion factor differs from the unit only for the longest estimated time, suggesting a higher disorder associated with this de-trapping path. Therefore, for the ZGO:Mn nanorods, the data are consistent with multi-trapping/de-trapping processes at different trap depths responsible for the distinct measured decays. Fig. 5-b) also shows afterglow images taken for ZGO and ZGO:Mn samples for 0 ms, 25 ms, and 50 ms after turning off the excitation source. When the lamp was turned off, it is clearly observable that both ZGO and ZGO:Mn exhibited intense bluish-white and green luminescence, respectively. While a fast intensity decay is seen for the blue light of the ZGO sample, the persistent Mn^{2+} GL is detected for longer times and with the used camera can no longer be detected for $t > 100$ ms.

4. Conclusions

Willemite-type nominal undoped, as well as Mn, and Cr-doped Zn_2GeO_4 prismatic nanorods, were successfully synthesized by microwave-assisted hydrothermal method at 170 °C. Despite the presence of larger agglomerates, the average dimensions of the as-synthesized nanorods were approximately 500 nm in length and around 150 nm in width. A thermal annealing treatment in air at 400 °C led to smoother surfaces, increased lengths, and reduced agglomerates. RT absorption spectra evidenced that the here studied samples have bandgap energy close to 5.25 eV. In addition, in the near band edge spectral region, broad absorption/excitation bands centered at 271 nm (~4.58 eV) and 315 nm (~3.94 eV) were assigned to an intrinsic defect and the Mn^{2+}-O^{2-} charge transfer state, respectively. For the case of the Cr-doped samples, the presence of trivalent and tetravalent ion charge states was identified, and the absorption bands were shown to be sensitive to the annealing temperature used. No red/NIR luminescence

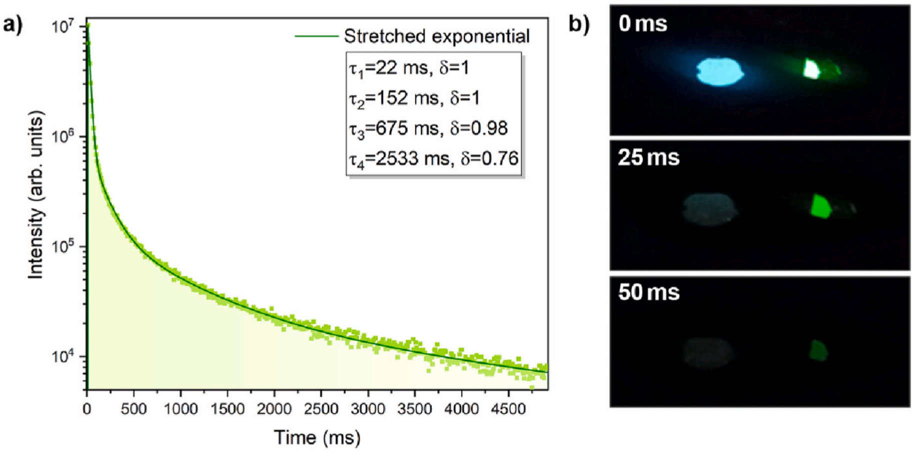

Fig. 5. a) Afterglow decay curve of the ZGO:Mn sample upon 10 min of excitation with 271 nm photons, and emission monitored at 535 nm; b) Afterglow photographs of the ZGO (left) and ZGO:Mn (right) samples at different times after the cessation of 10 min of excitation with 254 nm photons of a portable UV lamp.

related to intraionic Cr was observed at RT when exciting the samples at the Cr^{3+} and Cr^{4+} absorption bands. In contrast, when excitation photons with energy close to the bandgap energy and intrinsic defect absorption were used, a bright bluish-white emission was visible to the naked eye. This emission was proved to be due to the overlap of a blue-emitting intrinsic defect and the intraionic $^4T_1 \rightarrow ^6A_1$ Mn^{2+} green luminescence. The latter was also visible to the naked eye by exciting the Mn-doped samples either in the near band edge absorption or in the Mn^{2+}-O^{2-} charge transfer state. Temperature-dependent luminescence studies showed that when the excitation occurred in the charge transfer state, the non-radiative processes that compete with the Mn^{2+} luminescence in the synthesized doped nanorods could be described by a thermal activation energy of 18 ± 2 meV. In addition, persistent green luminescence from Mn^{2+} was observed for at least 5 s, with a kinetic described by a combination of four stretched exponentials. The data is consistent with multi-trapping/de-trapping processes at different trap depths responsible for the distinct measured decays. Based on the optical results obtained in this study, particularly its bright green persistent luminescence, the here-produced ZGO nanorods are a suitable material for anti-counterfeiting and security applications.

CRediT authorship contribution statement

Miguel P. Dias: Writing – review & editing, Writing – original draft, Investigation, Formal analysis. **Maria S. Batista:** Writing – review & editing, Investigation, Formal analysis, Data curation. **Ana Pimentel:** Writing – review & editing, Methodology, Investigation, Formal analysis. **Elvira Fortunato:** Writing – review & editing, Data curation. **Rodrigo Martins:** Writing – review & editing. **Florinda M. Costa:** Writing – review & editing, Formal analysis, Data curation. **Sónia O. Pereira:** Writing – review & editing, Supervision, Formal analysis, Data curation, Conceptualization. **Joana Rodrigues:** Writing – review & editing, Supervision, Methodology, Investigation, Formal analysis. **Teresa Monteiro:** Writing – review & editing, Writing – original draft, Validation, Supervision, Methodology, Data curation, Conceptualization.

Declaration of competing interest

The authors declare that they have no known competing financial interests or personal relationships that could have appeared to influence the work reported in this paper.

Acknowledgements

This study has the support of the Institute for Nanostructures, Nanomodelling and Nanofabrication (i3N), through projects UIDB/50025/2020–2023 & UIDP/50025/2020–2023 & LA/P/0037/2020, as well as IonProGO (2022.05329. PTDC), DOI: 10.54499/2022.05329, 2023.00054. RESTART, LIGHEART (2022.08597. PTDC) and, CO2RED (PTDC/EQU-EPQ/2195/2021) projects, all funded by the Foundation for Science and Technology (FCT). J. Rodrigues acknowledges FCT for Programme Stimulus of Scientific Employment–Individual Support (grant 2022.00010. CEECIND/CP1720/CT0023, DOI: 10.54499/2022.00010. CEECIND/CP1720/CT0023). M. S. Batista thanks i3N and FCT for the PhD grant (UI/BD/152567/2022). The authors thanks to MSc. Celeste Azevedo (CICECO – Aveiro Institute of Materials), for the DR experiments.

Data availability

Data will be made available on request.

References

[1] D. Gao, Q. Kuang, F. Gao, H. Xin, S. Yun, Y. Wang, Achieving opto-responsive multimode luminescence in $Zn_{1+x}Ga_{2-2}GeO_4$:Mn persistent phosphors for advanced anti-counterfeiting and information encryption, Mater. Today Phys. 27 (2022) 100765, https://doi.org/10.1016/j.mtphys.2022.100765.

[2] J. Huang, K. Ding, Y. Hou, X. Wang, X. Fu, Synthesis and photocatalytic activity of Zn_2GeO_4 nanorods for the degradation of organic pollutants in water, ChemSusChem 1 (2008) 1011–1019, https://doi.org/10.1002/cssc.200800166.

[3] J. Xue, F. Li, F. Liu, H.M. Noh, B.R. Lee, B.C. Choi, S.H. Park, J.H. Jeong, P. Du, Designing ultra-highly efficient Mn^{2+}-activated Zn_2GeO_4 green-emitting persistent phosphors toward versatile applications, Mater. Today Chem. 23 (2022) 100693, https://doi.org/10.1016/j.mtchem.2021.100693.

[4] Z. Wang, J. Wang, D. Gao, W. Xu, W. Gao, X. Zhang, S. Yun, X. Wang, Cr^{3+} -activated deep trap electron-trapping biphasic mixture of $Zn(Al,Ga)_2O_4$ and Zn_2GeO_4 for multilevel information storage by trap multiplexing and wavelength multiplexing, Luminescence 39 (2024) 1–8, https://doi.org/10.1002/bio.70027.

[5] S.K. Gupta, K. Sudarshan, B. Modak, R. Gupta, Interstitial zinc boosted light tunability, afterglow, and ultrabright white emission in zinc germanate (Zn_2GeO_4), ACS Appl. Electron. Mater. 5 (2023) 1286–1294, https://doi.org/10.1021/acsaelm.2c01759.

[6] J. Dolado, P. Hidalgo, B. Méndez, Correlative study of vibrational and luminescence properties of Zn_2GeO_4 microrods, Phys. Status Solidi 215 (2018) 1–5, https://doi.org/10.1002/pssa.201800270.

[7] S. Luo, L. Trefflich, S. Selle, R. Hildebrandt, E. Krüger, S. Lange, J. Yu, C. Sturm, M. Lorenz, H. von Wenckstern, C. Hagendorf, T. Höche, M. Grundmann, Ultrawide bandgap willemite-type Zn_2GeO_4 epitaxial thin films, Appl. Phys. Lett. 122 (2023), https://doi.org/10.1063/5.0130946.

[8] P. Hidalgo, A. López, B. Méndez, J. Piqueras, Synthesis and optical properties of Zn_2GeO_4 microrods, Acta Mater. 104 (2016) 84–90, https://doi.org/10.1016/j.actamat.2015.11.023.

[9] N.M. Cao Hoang Phuong Lan, C.X. Thang, V.-H.H. Pham, P. The Kien, V.T. Ngoc Minh, T.T. Hao Tam, Effects of Cr-doping on the morphology and optical properties in Zn_2GeO_4 (ZGO) nanorods prepared by hydrothermal method, Optik 199 (2019) 163310, https://doi.org/10.1016/j.ijleo.2019.163310.

[10] K.H. Yoon, J.H. Kim, Structural analysis and luminescent study of thin film zinc germanate doped with manganese, Thin Solid Films 519 (2010) 1583–1586, https://doi.org/10.1016/j.tsf.2010.08.157.

[11] D. Gao, F. Gao, Q. Kuang, X. Zhang, Z. Zhang, Y. Pan, R. Chai, H. Jiao, Zinc germanate nanophosphors with persistent luminescence for multi-mode imaging of latent fingerprints, ACS Appl. Nano Mater. 5 (2022) 9929–9939, https://doi.org/10.1021/acsanm.2c02163.

[12] R.T. Parayil, S.K. Gupta, M. Mohapatra, A review on defect engineered NIR persistent luminescence through transition metal ion (Cr, Mn, Fe and Ni) doping: wider perspective covering synthesis, characterization, fundamentals and applications, Coord. Chem. Rev. 522 (2025) 216200, https://doi.org/10.1016/j.ccr.2024.216200.

[13] Z. Gu, F. Liu, X. Li, Z.W. Pan, Luminescent Zn_2GeO_4 nanorod arrays and nanowires, Phys. Chem. Chem. Phys. 15 (2013) 7488, https://doi.org/10.1039/c3cp43977a.

[14] J. Dolado, J. García-Fernández, P. Hidalgo, J. González-Calbet, J. Ramírez-Castellanos, B. Méndez, Intense cold-white emission due to native defects in Zn_2GeO_4 nanocrystals, J. Alloys Compd. 898 (2022) 162993, https://doi.org/10.1016/j.jallcom.2021.162993.

[15] Q. Zhang, J. Wang, Synthesis and characterization of Zn_2GeO_4:Mn^{2+} phosphor for field emission displays, Appl. Phys. A 108 (2012) 943–948, https://doi.org/10.1007/s00339-012-7003-6.

[16] S. Takeshita, J. Honda, T. Isobe, T. Sawayama, S. Niikura, Solvothermal synthesis of Zn_2GeO_4:Mn^{2+} nanophosphor in water/diethylene glycol system, J. Solid State Chem. 189 (2012) 112–116, https://doi.org/10.1016/j.jssc.2011.12.001.

[17] F. Chi, X. Wei, B. Jiang, Y. Chen, C. Duan, M. Yin, Luminescence properties and the thermal quenching mechanism of Mn^{2+} doped Zn_2GeO_4 long persistent phosphors, Dalton Trans. 47 (2018) 1303–1311, https://doi.org/10.1039/C7DT03906A.

[18] M. Yang, Y. Ji, W. Liu, Y. Wang, X. Liu, Facile microwave-assisted synthesis and effective photocatalytic hydrogen generation of Zn_2GeO_4 with different morphology, RSC Adv. 4 (2014) 15048–15054, https://doi.org/10.1039/C4RA01041H.

[19] P. Kubelk, F. Munk, A contribution to the optics of pigments, Z. Technol. Phys. 12 (1931) 593–601.

[20] P. Makuła, M. Pacia, W. Macyk, How to correctly determine the band gap energy of modified semiconductor photocatalysts based on UV–vis spectra, J. Phys. Chem. Lett. 9 (2018) 6814–6817, https://doi.org/10.1021/acs.jpclett.8b02892.

[21] S. He, Y. Liu, T. Gao, R. Liu, G. Chen, M. Duan, M. Cao, Enhanced luminescence of long-wavelength broadband near-infrared germanate phosphors, ACS Omega 8 (2023) 15698–15707, https://doi.org/10.1021/acsomega.3c00995.

[22] Y. Cong, Y. He, B. Dong, Y. Xiao, L. Wang, Long afterglow properties of Zn_2GeO_4:Mn^{2+}, Cr^{3+} phosphor, Opt. Mater. 42 (2015) 506–510, https://doi.org/10.1016/j.optmat.2015.01.045.

[23] Y. Zhao, S. Yang, J. Zhu, G. Ji, F. Peng, The study of oxygen ion motion in Zn_2GeO_4 by Raman spectroscopy, Solid State Ionics 274 (2015) 12–16, https://doi.org/10.1016/j.ssi.2015.02.015.

[24] B. Henderson, G.F. Imbusch, Optical Spectroscopy of Inorganic Solids, Oxford University Press, New York, 1989.

[25] Y. Tanabe, S. Sugano, On the absorption spectra of complex ions, III the calculation of the crystalline field strength, J. Phys. Soc. Japan 11 (1956) 864–877, https://doi.org/10.1143/JPSJ.11.864.

[26] Y. Zhuang, S. Tanabe, J. Qiu, Wavelength tailorability of broadband near-infrared luminescence in Cr^{4+}-activated transparent glass-ceramics, J. Am. Ceram. Soc. 97 (2014) 3519–3523, https://doi.org/10.1111/jace.13128.

[27] J. Dolado, R. Martínez-Casado, P. Hidalgo, R. Gutierrez, A. Dianat, G. Cuniberti, F. Domínguez-Adame, E. Díaz, B. Méndez, Understanding the UV luminescence of zinc germanate: the role of native defects, Acta Mater. 196 (2020) 626–634, https://doi.org/10.1016/j.actamat.2020.07.009.

[28] I. Pelant, J. Valenta, Luminescence Spectroscopy of Semiconductors, Oxford University PressOxford, 2012, https://doi.org/10.1093/acprof:oso/9780199588336.001.0001.